NANO: Brief Reports and Reviews
Vol. 17, No. 3 (2022) 2250025 (9 pages)

DOI: 10.1142/S1793292022500254

World Scientific
www.worldscientific.com

Mixed-Phase TiO_2 with Oxygen Vacancies for Enhanced Visible Light Photocatalysis Performance

Xi Chen*, Tian-Song Deng*,†,‡, Ming Zhou*, Zhihua Dong* and Zhiqun Cheng*
*College of Electronics and Information Engineering
Hangzhou Dianzi University
Hangzhou 310018, P. R. China
†dengts@pku.edu.cn

Received 4 November 2021
Accepted 13 March 2022
Published 21 April 2022

Because of the decrease in the band gap and the carrier recombination rate, the visible light photocatalysis performance of the mixed-phase TiO_2 with oxygen vacancies is better than that of the pure-phase TiO_2. In this study, two different acids were separately applied in the hydrothermal synthesis of TiO_2 nanoparticles without any post-heat treatment. The reaction was carried out at a relatively low temperature not exceeding 140°C. Both kinds of crystallized TiO_2 powders show much more band gap reduction than that of commercial Degussa P25 TiO_2 nanoparticles, which can be attributed to the oxygen vacancies. Under the visible light illumination-assisted photocatalytic degradation of methyl orange in water, the two mixed-phase TiO_2 powders exhibited a steady photocatalytic activity upon increasing to five cycles. The highest photocatalytic efficiency of the two powders is 2.7 times than that of the P25 powder, which is regarded as an excellent photocatalyst for water purification.

Keywords: TiO_2 nanoparticles; mixed phase; oxygen vacancies; visible-light photocatalytic activity; hydrothermal synthesis.

1. Introduction

Titanium dioxide (TiO_2) is probably the most well known and has been widely applied in different fields, such as photocatalysis,[1] sensors,[2] batteries[3] and supercapacitors.[4] Due to its advantages of low-cost, high chemical stability, nontoxicity, environmental-friendly and the ability to degrade a variety of pollutants, TiO_2 has been a kind of widely investigated wide-bandgap semiconductor materials (3.2 eV for anatase and 3.0 eV for rutile) and under UV light illumination, TiO_2 has an excellent photocatalyst performance.[1,5] TiO_2 nanoparticles have excellent photocatalytic activities and are the most widely used photocatalytic materials nowadays. One of them is the well-known commercial Degussa P25 TiO_2 nanoparticles, which usually serve as a benchmark for evaluating the activity of new photocatalysts.[6,7] However, owing to the rapid recombination of electron-hole pairs, the low efficiency of TiO_2 under visible-light illumination limits its wide application in pollutants degradation.[5,7]

Over the past decade, numerous methods have been proposed to enhance the visible-light photocatalytic activity of TiO_2 powders, such as the

‡Corresponding author.

construction of the mixed-phase TiO_2 and the introduction of oxygen vacancies.[8–12] According to previous studies, TiO_2 containing both anatase and rutile phases always shows much higher photocatalytic activity than TiO_2 with pure anatase phase or rutile phase.[5,8,13] In addition, the commercial Degussa P25 composed of 80% anatase and 20% rutile is considered as a potential photocatalyst.[5] The internal built-in electric field up to 1 kV/cm is formed between anatase and rutile phases cross-section with the direction from anatase to rutile.[13,14] The phase junction plays a decisive role in promoting the rapid transfer of electrons and holes, leading to efficient separation of carriers and then prolonging charge lifetimes, resulting in greater photocatalytic reactivity.[13–15] In general, the conversion of titanite to TiO_2, crystallization process of TiO_2 and construction of phase junction in TiO_2 all demand heat treatment. However, high temperature calcination often leads to particle growth, hydroxyl groups loss and repugnant agglomerations, thus resulting in the decline of photocatalytic activity.

Defects have been proved to effectively regulate the performance of semiconductors, such as oxygen vacancies as an important strategy for adjusting the band gap.[10,16,17] Previous studies have shown that the band gap narrowed and visible light adsorption range expanded by introducing the defect level or shallow donor level.[16,18,19] This is owing to the shift of Fermi level toward the conduction band due to the existence of oxygen vacancy. In addition, the density of states below the Femi energy level caused by oxygen vacancies significantly promotes the effective separation of the carriers.[20,21] Therefore, the introduction of appropriate oxygen vacancies is an effective way to improve the visible-light photocatalytic activity.

It is still a major challenge to explore a simple method to simultaneously construct a mixed phase with efficient phase junction and introduce oxygen vacancies at relatively lower temperature. In this paper, mixed-phase TiO_2 nanoparticles with high crystallinity were synthesized by a simple and mild acid-assisted hydrothermal method. Titanium butoxide (TBT) was used as titanium source and hydrochloric acid or acetic acid as auxiliary to promote the formation of the mixed-phase and introduce the oxygen vacancies. The mixed-phase TiO_2 nanoparticles showed higher visible light photocatalytic activity than that of P25 in the degradation of methyl orange (MO) in water under visible light illumination. The current synthetic route does not need high temperature treatment. In addition, the visible light photocatalytic activity of the mixed-phase TiO_2 powders prepared by two acids were indeed investigated, which provides more choices for commercial production of TiO_2 nanoparticles in the future.

2. Experimental

2.1. *Materials*

Titanium butoxide, ethanol (99.7%), acetic acid (99.5%) and MO (96%) were purchased from Shanghai Macklin Biochemical Technology Co., Ltd. Hydrochloric acid (37%) was purchased from Hangzhou Jiachen Chemical Co., Ltd. All chemicals were of analytical grade and used without further purifications.

2.2. *Preparation of TiO_2 nanoparticles*

In a beaker, 5 mL of titanium butoxide (TBT) to 120 mL ethanol was slowly added under continuous stirring, and then continuously stirred for 30 min to form a homogeneous solution A. Solution B was either 64 mL 0.78 M hydrochloric acid (HCl) aqueous solution or 72 mL 2.91 M acetic acid (CH_3COOH) aqueous solution. Under continuous stirring, solution B was added dropwise to solution A, and then continuously stirred for 30 min to form solution C. Then, the mixed solution C was transferred into a Teflon-lined autoclave for further hydrothermal reaction at 140°C for 4 h to complete the precipitation process. The precipitates were collected by centrifugation, washed alternatively with distilled water and ethanol for three times and dried in air at 80°C overnight for further characterizations and photocatalytic experiments. The TiO_2 nanoparticles obtained from HCl and CH_3COOH were termed as H-TiO_2 and A-TiO_2, respectively. The benchmark TiO_2 photocatalyst (P25) was used as the comparison in this study.

2.3. *Characterizations*

X-ray diffraction (XRD) measurements were performed on an XRD diffractometer (Rigaku SmartLab 9 kW) using Cu Kα radiation, operated at 40 kV and 100 mA ($\lambda = 0.15406$ nm). X-ray photoelectron spectroscopy (XPS) using Al Kα

radiation ($h\upsilon = 1486.6$ eV) as the X-ray source was carried out using the AXIS Supra system (Kratos, UK) at 150 W and 15.0 kV. The spectra were corrected by C 1s (284.6 eV) bond. The morphology was observed by a field emission scanning electron microscopy (FESEM, ApreoS HiVac). High resolution transmission electron microscopy (HRTEM) was performed on a FEI Talos F200S operated at 200 kV. Electron spin-resonance spectroscopy (ESR) spectra of the samples were recorded on a Bruke EMXplus in air at room temperature. Fourier transform infrared spectroscopy (FTIR) experiments were carried out with an IR Prestige-21 spectrometer (Japan), the functional groups contained in the material were analyzed by spectrogram and the compound structure of the sample was inferred. When measuring the samples with Fourier infrared, ensure that the sample is completely dry. UV-Vis absorption spectra were collected using a UV-Vis near-infrared spectrometer (UV-1900i, Shimadzu). The low-temperature N_2 adsorption–desorption analysis was performed at 77 K using an Autosorb-IQ2-MP (Quantachrome Instruments). The specific surface area (SSA) was calcinated by the Brunauer–Emmette–Teller (BET) method using adsorption data and the SSA was measured at a relative pressure lower than 0.3. The pore-sized distribution was measured by the Barrett–Joyner–Halenda (BJH) method. Before measurement, degassing was carried out in vacuum of 80°C for 25 h to remove the physically absorbed gas.

2.4. *Photocatalytic activity evaluations*

Under visible light irradiation, the photocatalytic degradation of MO in water with an initial concentration of 0.01 mM was studied, and its photocatalytic performance was evaluated. A 250 W Xenon lamp (HDL-II, Suzhou Betical Optoelectronics Technology Co., Ltd., China) was used as the light source, equipped with a filter in which the light less than 420 nm was cut off. In a typical procedure, a certain amount of catalyst (200 mg) was placed in 100 mL MO aqueous solution (20 mg/L). The suspension was stirred in dark for several hours to achieve an adsorption–desorption equilibrium, and then placed under visible light illumination with an intensity of ca. 200 mW/cm^2. 1.5 mL suspension for sampling was taken out at regular intervals. After removing the powders by centrifugation, the dye concentration was determined at the wavelength of 465 nm using a UV-Vis spectrophotometer (UV-1900i, Shimadzu). The photodegradation reaction was maintained at normal atmospheric temperature. The cycling performance test was carried out under the same conditions.

3. Results and Discussion

In order to clearly determine the crystalline structures and phase purities of the samples, XRD characterization was carried out. The differences in crystalline and structure between the H-TiO_2, A-TiO_2 and P25 samples could be observed via XRD [Figs. 1(a) and 1(b)]. As shown in Fig. 1(a), all samples exhibit typical diffractions peaks related to pure TiO_2. The peaks of the A-TiO_2 and P25 can be labeled as well-crystallized anatase (JCPDS No. 21–1272) and rutile (JCPDS No. 21–1276). The HCl-assisted hydrothermal synthesis resulted in the formation of a mixture of anatase, rutile and brookite (JCPDS No. 29–1360) in the H-TiO_2 nanoparticles. The diffraction peaks were observed at 25.28, 37.70, 48.05, 53.89, 55.06, 62.69, 68.76, 70.31 and 75.03° and were marked into the (101), (004), (200), (105), (211), (204), (116), (220) and (215) planes of anatase TiO_2, respectively. The XRD patterns of H-TiO_2 samples show a peak at 30.80°, which was consistent with the (121) plane of brookite TiO_2. This means that the special mixed phase of H-TiO_2 is helpful to improve photocatalytic activity. This heterojunction structure of TiO_2 with anatase, rutile and brookite phase could further reduce the photogenerated carriers recombination rate.[22,23]

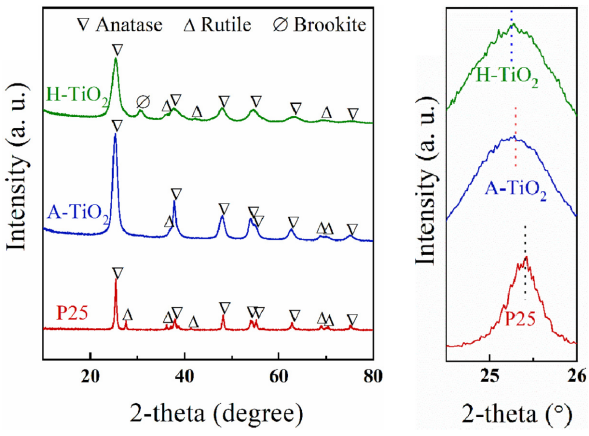

Fig. 1. (a) XRD patterns and (b) partial XRD patterns of H-TiO_2, A-TiO_2 and P25.

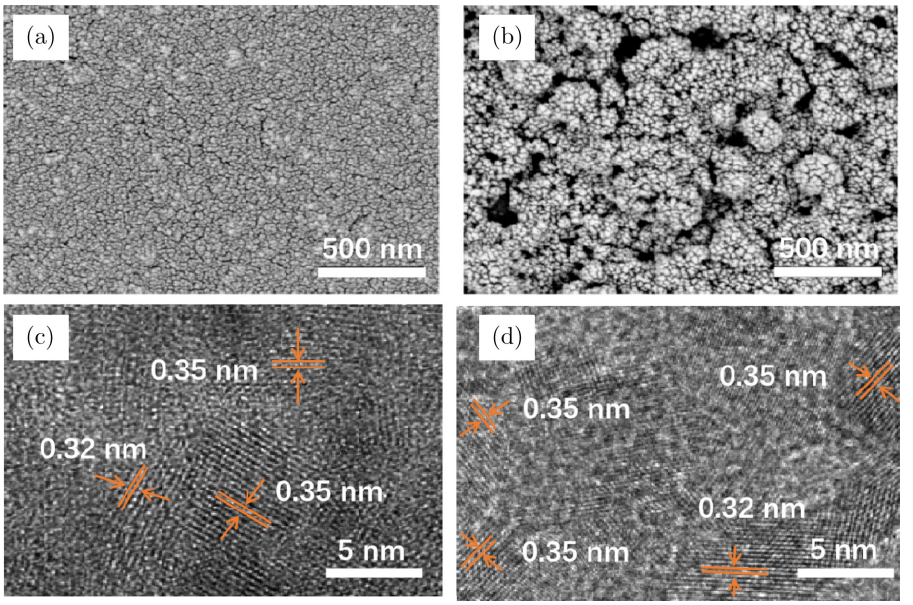

Fig. 2. FESEM images of the TiO_2 nanoparticles obtained from different acid: (a) HCl (H-TiO_2), (b) CH_3COOH (A-TiO_2). HRTEM images of (c) H-TiO_2, (d) A-TiO_2. Lattice spaces were labeled in HRTEM images.

However, anatase $TiO_2$with the peaks at 25.28° show a slight shift to lower angles compared to that of P25 [Fig. 1(b)] in the pattern of A-TiO_2 and H-TiO_2 samples, indicating that the lattice of A-TiO_2 and H-TiO_2 samples prepared by the acid-assisted hydrothermal synthesis is increased in this work.

The morphology of TiO_2 nanoparticles was characterized by SEM and TEM (Figs. 2 and S1). TiO_2 nanoparticles obtained by HCl [H-TiO_2, Fig. 2(a)] and CH_3COOH [A-TiO_2, Fig. 2(b)] assistant hydrothermal method, respectively, show different morphologies from P25 (Fig. S1). Compared with the morphology and structure of P25 nanoparticles, that of H-TiO_2 and A-TiO_2, show much higher uniformity. Both the size of the H-TiO_2 and A-TiO_2 nanoparticles are smaller than that of P25. The H-TiO_2 shows the best dispersibility of the three samples shown in Fig. 2(a). A-TiO_2 shows less agglomeration than P25 powders [Figs. 2(b) and S1]. Generally, the more the catalyst agglomeration, the worse the photocatalytic performance.[5,24] The HRTEM was used to determine the crystalline structures of the H-TiO_2 and A-TiO_2 [Figs. 2(c) and 2(d)]. Two types of lattice spaces were observed, 0.35 nm corresponding to {101} facet of anatase phase and 0.32 nm to {110} facet of rutile phase. Both the XRD and HRTEM analysis indicated mixed phase of the obtained TiO_2 nanoparticles.

The detailed surface analysis of the H-TiO_2, A-TiO_2 and P25 samples is carried out by XPS. Figures 3(a) and 3(b) reveal the high-resolution Ti 2p and O 1 s XPS spectra. For all the powder samples, the XPS spectrum of Ti 2p shows two peaks corresponding to Ti 2p1/2 and Ti 2p3/2, splitting into 5.7 eV, which is characteristic of Ti^{4+} in the TiO_2 lattice.[7,25] According to the XRD results, compared to the spectra of the P25, the positions of the Ti 2p3/2 and Ti 2p1/2 peaks of the H-TiO_2 and A-TiO_2 samples were moved slightly to lower binding energy, indicating the formation of low valence titanium,[8] which could lead to lattice expansion. For the O1s peak, the spectra can be fitted into two peaks. The peak with lower binding energy is related to the Ti-O bonds in crystalline TiO_2 and the peak with higher binding energy is related to the surface hydroxyl groups.[7,8,25] The amount of hydroxyl groups in the total oxygen components of samples can be determined by the ratio of the integrated area of two peaks.[7] The hydroxyl peak area ratio of H-TiO_2 powder is 0.35, which is significantly higher than 0.24 of the A-TiO_2 powder and 0.22 of the P25 powder. These results ensure a high percentage of surface hydroxyl groups. Therefore, acid-assisted hydrothermal synthesis can be considered a simple strategy to introduce oxygen vacancy defects in the original TiO_2. The results are consistent with the XRD analysis.

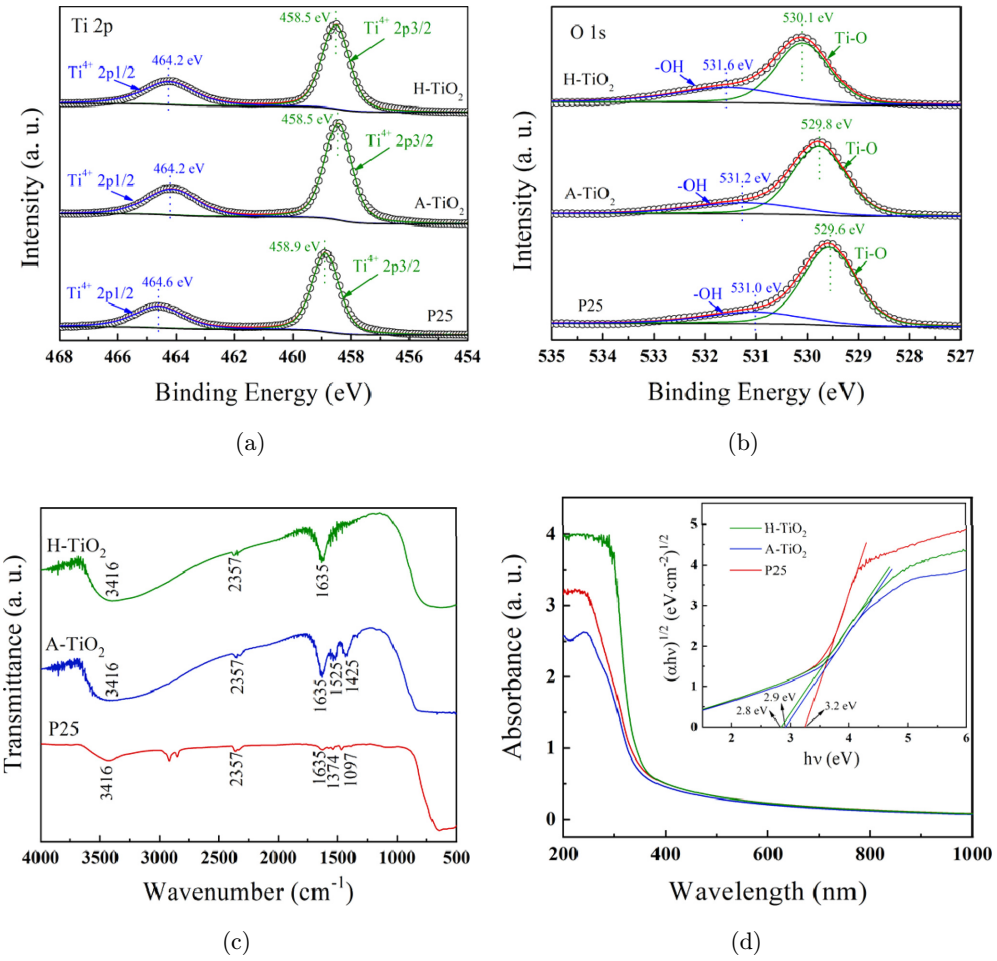

Fig. 3. (a, b) XPS spectra of H-TiO_2, A-TiO_2 and P25 nanoparticles: (a) Ti 2p and (b) O 1s spectra. (c) FTIR spectra of H-TiO_2, A-TiO_2 and P25 nanoparticles. (d) UV-Vis diffuse absorbance spectra of the H-TiO_2, A-TiO_2 and P25 nanoparticles, the inset replotting of the $(\alpha h\nu)^{1/2} \sim h\nu$ coordinate to evaluate the band gap.

In order to further determine the surface functional groups of the H-TiO_2, A-TiO_2 and P25 samples, FTIR experiments were carried out. The FTIR spectra are shown in Fig. 3(c). Obviously, H-TiO_2 and A-TiO_2 exhibit stronger −OH stretching bands than that of P25. As reported in previous works,[8,22,26] the dissociative adsorption of water is more likely to bond with oxygen vacancies, resulting in more hydroxyl groups on the surface of TiO_2. The abundant surface hydroxyl groups [Fig. 3(c)] act as capture centers for photoinduced electrons.[7,22,26] Therefore, electrons and holes are effectively separated.[27,28] The optical properties of the H-TiO_2, A-TiO_2 and P25 samples are evaluated by UV-Vis absorption spectra in Fig. 3(d). The band gaps of the H-TiO_2, A-TiO_2 and P25 samples were evaluated by UV-Vis diffuse reflectance spectra based on the Kubelka–Munk function, assuming that there is an indirect transition between the valance and conduction bands for TiO_2.[5] The band gaps of H-TiO_2, A-TiO_2 and P25 samples are estimated to be 2.8 eV, 2.9 eV and 3.2 eV, respectively [Fig. 3(d)]. Owing to the existence of mixed-phase junction and oxygen vacancies, the band gap of the H-TiO_2 and A-TiO_2 powders is reduced compared with P25. It should be noted that surface hydroxyl groups generally are usually produced owing to the dissociation and adsorption of water molecules on the TiO_2 surface during hypoxia; therefore, the abundant surface hydroxyl groups as shown in Fig. 3(c) strongly implies of surface hypoxia. H-TiO_2 and A-TiO_2 powders have better visible-light photocatalytic performance than P25, which may be owing to the successful reduction of the band gap.[29–31] In the meantime, the absorption edge of H-TiO_2 further red shifted compared with P25 and A-TiO_2 [Fig. 3(d)]. As previously reported, the formation of defect energy level in the H-TiO_2 band

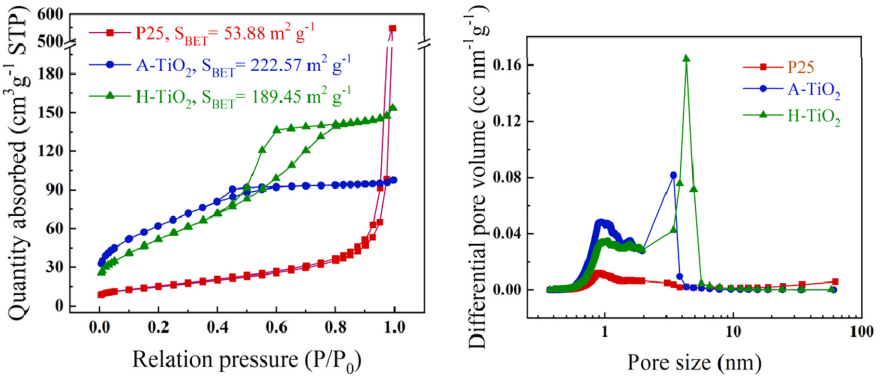

(a) (b)

Fig. 4. (a) The low-temperature nitrogen adsorption–desorption isotherms of the P25 and A-TiO_2 and H-TiO_2 nanoparticles; (b) the corresponding pore-size distribution curves.

gap leads to the red shifted of absorption edge.[5,7,24] The ESR spectra (Fig. S2) showed that the two samples all gave rise to a signal peak at $g = 2.003$, corresponding to bulk SETOV.[7,23] Comparing the two SETOV peaks of H-TiO_2 and A-TiO_2, we found that the SETOV peak intensity of A-TiO_2 was much higher than H-TiO_2. H-TiO_2 and A-TiO_2have a weak signal peak at $g = 2.02$, which is considered to be the signal peak of O^{2-}. This is because Ti^{3+} on surface can reduce the adsorption of O_2 in the atmosphere of O^{2t}. The results showed that the oxygen vacancy on TiO_2 surface usually had two electrons or no electrons, but ESR could not detect the signal of these two oxygen vacancies directly. Ti^{4+} can be reduced from an oxygen vacancy with two electrons to Ti^{3+} by capturing electrons, so the formation of Ti^{3+} can indirectly verify the existence of an oxygen vacancy on the surface. However, the catalytic performance of H-TiO_2 is better than that of A-TiO_2. Combining the XRD and XPS results, we guess that the catalytic performance is not only related to the oxygen vacancy, but also to the special mixture phase of H-TiO_2 and its less agglomeration.[23,31]

The low-temperature N_2 adsorption–desorption isotherm of the P25 and A-TiO_2 and H-TiO_2 nanoparticles are shown in Fig. 4(a). The BET SSA of the P25, A-TiO_2 and H-TiO_2 samples is determined to be $53.88\,m^2/g$, $222.57\,m^2/g$ and $189.45\,m^2/g$, respectively. The nanoparticles of A-TiO_2 and H-TiO_2 have much higher SSA than P25. These results show that the SSA can be significantly improved by acid-assisted hydrothermal synthesis to achieve small and homogeneity TiO_2 nanoparticles. Dye molecules will increase more contact owing to the large SSA.[32,33] The corresponding average pore size of H-TiO_2, A-TiO_2 and P25 samples are $62.80\,m^2/g$, $2.71\,m^2/g$ and $5.02\,m^2/g$, respectively, with the total pore volume of $0.85\,cm^3/g$, $0.15\,cm^3/g$ and $0.24\,cm^3/g$. The high visible light photocatalytic performance can be improved by appropriate pore size and total pore volume.

The photocatalytic activity of the P25, A-TiO_2 and H-TiO_2 powders was evaluated by photodegradation of MO in water under the illumination of visible light, and the results are displayed in Fig. 5(a). Under the same conditions, the H-TiO_2 powder has the highest activity compared with the A-TiO_2 and P25 powders. With the help of H-TiO_2 powder, the dye molecules degraded 95% of the initial amount within 4 h while A-TiO_2 degrades 76% and P25 only 36% of initial MO molecules in the same time. Figure 5(b) shows that all the degradation processes could be well fitted by the pseudo-first-order kinetics.[1,5,22] The reaction rate constants of H-TiO_2, A-TiO_2 and P25 samples are $0.014\,min^{-1}$, $0.005\,min^{-1}$ and $0.002\,min^{-1}$, respectively. The H-TiO_2 and A-TiO_2 of the study exhibited efficiencies better than that of P25. The reaction rate constant of H-TiO_2 is almost three times that of A-TiO_2 nanoparticles and seven times that of P25 powder. The photocatalytic activity was significantly improved by the mixed phase and oxygen vacancies.

The stability of the P25 [Fig. 6(a)], A-TiO_2 [Fig. 6(b)] and H-TiO_2 [Fig. 6(c)] nanoparticles was confirmed by repetitively degrading MO in water under the illumination of visible light for up to five cycles. The photocatalytic capacity of all samples showed better and better. This is because of the

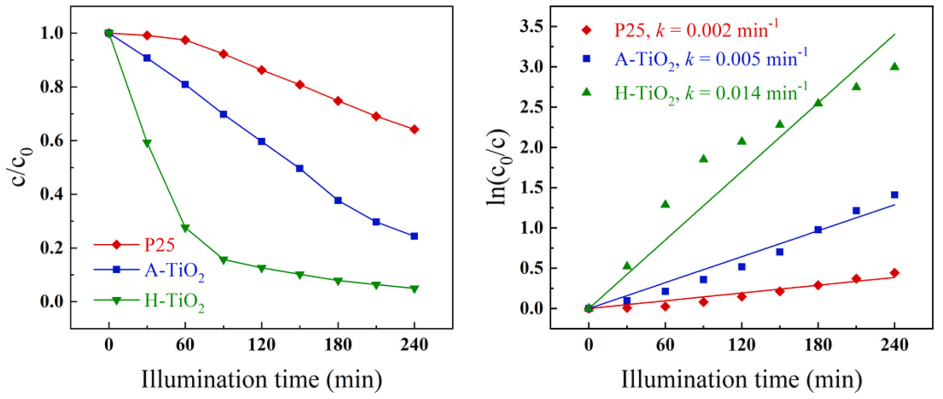

(a) (b)

Fig. 5. Photodegradations of MO in the presence of the P25, A-TiO_2 and H-TiO_2 nanoparticles under visible-light illumination: (a) the degradation curves; (b) the fitting results assuming a pseudo-first-order reaction.

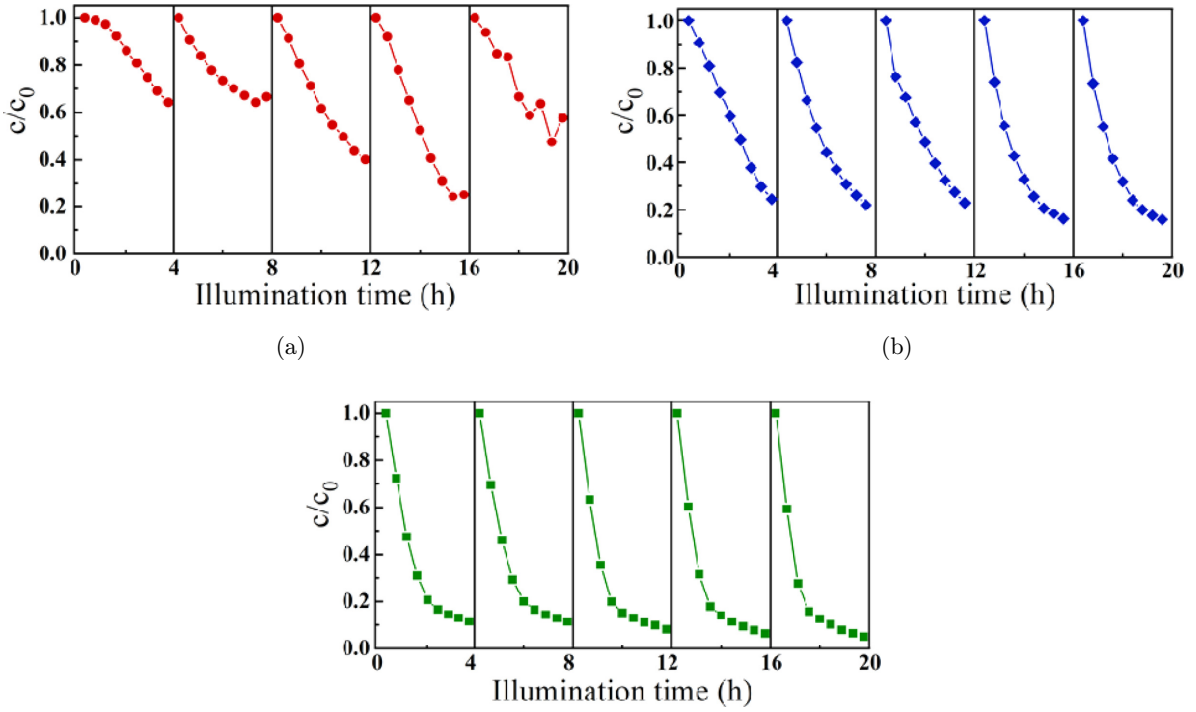

(a) (b)

(c)

Fig. 6. The cycling photodegradations of MO in the presence of the (a) P25, (b) A-TiO_2 and (c) H-TiO_2 nanoparticles under visible-light illumination.

catalyst loss after the recycling and the initial concentration of MO is reduced in the same proportion when the same visible light source is used. It should be noted that the photocatalytic capacity of H-TiO_2 and A-TiO_2 is more stable than P25. This is owing to the large SSA,[30,33,34] which can reduce band gap and increase the light capture,[33,34] while the abundant surface hydroxyl groups acted as capture centers for photoinduced electrons.[23,24]

4. Conclusion

We have demonstrated that mixed-phase TiO_2 nanoparticles can be synthesized by acid-assisted

hydrothermal synthesis at 140°C without any post-calcination. TiO_2 samples synthesized using HCl or CH_3COOH have uniform nanoparticle morphology and good monodispersity. Compared with P25, the SSA of the H-TiO_2 and A-TiO_2 is larger. At the same time, due to the rich surface hydroxyl groups generated by oxygen vacancies, the band gap generated by mixed phase is reduced, which ensures that H-TiO_2 and A-TiO_2 have excellent photocatalytic performances when assisting in the degradation of MO in water under visible light illumination. The stable high photocatalytic performance and the simple preparation methods of the H-TiO_2 and A-TiO_2 nanoparticles will promote the industrial application.

Acknowledgments

We thank Dr. Jia Liu for high resolution transmission electron microscopy (HRTEM) support. The authors acknowledge financial support from the National Natural Science Foundation of China (NSFC, Grant No. 61905056). This work was also supported by the National Key R&D Program of China (Grant No. 2018YFE0207500), the National Natural Science Foundation (Grant Nos. 91938201 and 61871169), Zhejiang Provincial Natural Science Foundation (Grant No. LZ20F010004) and Project of Ministry of Science and Technology (Grant No. D20011).

References

1. X. Han *et al.*, *Appl. Catal. B Environ.* **265**, 118539 (2020), doi: 10.1016/j.apcatb.2019.118539.
2. A. Giampiccolo *et al.*, *Appl. Catal. B Environ.* **243**, 183 (2019), doi: 10.1016/j.apcatb.2018.10.032.
3. Q. Ni *et al.*, *Energy Storage Mater.* **25**, 903 (2020), doi: 10.1016/j.ensm.2019.09.001.
4. Y. J. Gu, W. Wen and J. M. Wu, *J. Power Sources* **469**, 228425 (2020), doi: 10.1016/j.jpowsour.2020.228425.
5. W. Zhang *et al.*, *Adv. Energy Mater.* **11**, 2003303 (2020), doi: 10.1002/aenm.202003303.
6. Q. Wang *et al.*, *Solid State Sci.* **77**, 14 (2018), doi: 10.1016/j.solidstatesciences.2018.01.003.
7. L. L. Lai, W. Wen and J. M. Wu, *Chemistry Select* **2**, 5025 (2017), doi: 10.1002/slct.201700372.
8. M. Du *et al.*, *J. Alloys Compd.* **830**, 154649 (2020), doi: 10.1016/j.jallcom.2020.154649.
9. L. Yang *et al.*, *J. Hazard Mater.* **365**, 107 (2019), doi: 10.1016/j.jhazmat.2018.10.090.
10. X. Song *et al.*, *J. Energy Chem.* **55**, 154 (2021), doi: 10.1016/j.jechem.2020.07.013.
11. X. Y. Chen *et al.*, *Chem. Eng. J.* **427**, 130945 (2022), doi: 10.1016/j.cej.2021.130945.
12. X. Y. Feng *et al.*, *Chem. Eng. J.* **352**, 947 (2018), doi: 10.1016/j.cej.2018.06.037.
13. X. Wang and C. Li, *J. Phys. Chem. C* **122**, 21083 (2018), doi: 10.1021/acs.jpcc.8b06039.
14. Y. Guo *et al.*, *Appl. Catal. B Environ.* **262**, 118262 (2020), doi: 10.1016/j.apcatb.2019.118262.
15. Y. Gao *et al.*, *J. Phys. Chem. Lett.* **8**, 1419 (2017), doi: 10.1021/acs.jpclett.7b00285.
16. J. Xiong *et al.*, *Adv. Funct. Mater.* **28**, 1801983 (2018), doi: 10.1002/adfm.201801983.
17. T. Wu *et al.*, *Adv. Mater.* **32**, 2000299 (2020), doi: 10.1002/adma.202000299.
18. X. Lang *et al.*, *J. Phys. Chem. C* **121**, 6072 (2017), doi: 10.1021/acs.jpcc.6b11356.
19. R. Chen *et al.*, *Nano Lett.* **19**, 426 (2019), doi: 10.1021/acs.nanolett.8b04245.
20. P. F. Zhu *et al.*, *Chin. J. Catal.* **42**, 175 (2021), doi: 10.1016/S1872-2067(20)63592-6.
21. Y. J. Gu *et al.*, *Appl. Surf. Sci.* **434**, 1055 (2018), doi: 10.1016/j.apsusc.2017.10.216.
22. R. Jiang, W. Wen and J. M. Wu, *New J. Chem.* **42**, 3020 (2018), doi: 10.1039/c7nj04628f.
23. F. Y. Xu *et al.*, *Int. J. Hydrogen Energy* **28**, 15394 (2014), doi: 10.1016/j.ijhydene.2014.07.166.
24. Y. Xu *et al.*, *Mater. Chem. Front.* **1**, 1453 (2017), doi: 10.1039/c7qm00019g.
25. W. Ouyang *et al.*, *J. Alloy Compd.* **866**, 158964 (2021), doi: 10.1016/j.jallcom.2021.158964.
26. T. Zhang *et al.*, *Chem. Eng. J.* **384**, 123350 (2020), doi: 10.1016/j.cej.2019.123350.
27. X. He *et al.*, *J. Hazard Mater.* **403**, 124048 (2021), doi: 10.1016/j.jhazmat.2020.124048.
28. G. K. Upadhyay *et al.*, *Mater. Chem. Phys.* **253**, 123191 (2020), doi: 10.1016/j.matchemphys.2020.123191.
29. X. Feng *et al.*, *J. Hazard Mater.* **351**, 196 (2018), doi: 10.1016/j.jhazmat.2018.03.013.
30. X. Chen *et al.*, *Colloids Surf. A* **603**, 125188 (2020), doi: 10.1016/j.colsurfa.2020.125188.
31. L. L. Hou *et al.*, *Appl. Surf. Sci.* **428**, 640 (2018), doi: 10.1016/j.apsusc.2017.09.144.
32. X. Liu and C. Chen, *Mater. Lett.* **261**, 127127 (2020), doi: 10.1016/j.matlet.2019.127127.
33. J. Chen *et al.*, *Nanoscale* **12**, 3574 (2020), doi: 10.1039/c9nr08542d.
34. Y. Yue *et al.*, *J. Hazard Mater.* **384**, 121302 (2020), doi: 10.1016/j.jhazmat.2019.121302.

Supporting Information

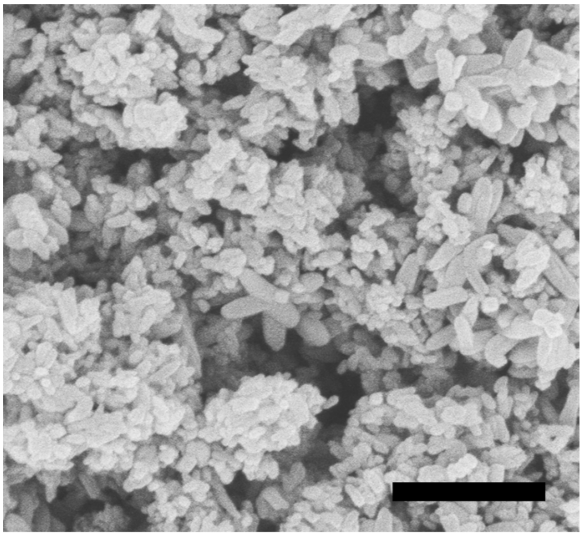

Fig. S1. FESEM image of the P25 nanoparticles. The scale bar is 500 nm.

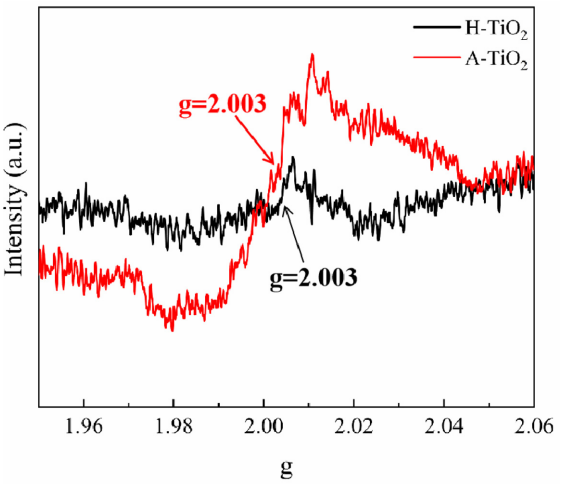

Fig. S2. ESR spectra of the H-TiO_2 and A-TiO_2.